

Photo-electrochemical Characterization of New Lead-free Ferroelectric $\text{Ba}_{0.975}\text{Ho}_{0.017}(\text{Zr}_{0.2}\text{Ti}_{0.75})\text{Sn}_{0.05}\text{O}_3$ Ceramic. Application to Bezacryl Oxidation Under Solar Light

S. Smail

USTHB: Universite des Sciences et de la Technologie Houari Boumediene

Gharib Rekhila (✉ rekhilagharib@gmail.com)

Laboratory of Storage and Valorization of Renewable Energies <https://orcid.org/0000-0003-2257-0162>

K. Taïbi

USTHB: Universite des Sciences et de la Technologie Houari Boumediene

A. Lahmar

LPMC: Institut Charles Gerhardt de Montpellier

M. Trari

USTHB: Universite des Sciences et de la Technologie Houari Boumediene

Original Research

Keywords: relaxor $\text{Ba}_{0.975}\text{Ho}_{0.017}(\text{Zr}_{0.2}\text{Ti}_{0.75})\text{Sn}_{0.05}\text{O}_3$, Dielectric , Photocatalysis, Bezacryl , Solar light,

Posted Date: February 17th, 2021

DOI: <https://doi.org/10.21203/rs.3.rs-203322/v1>

License:   This work is licensed under a Creative Commons Attribution 4.0 International License.

[Read Full License](#)

**Photo-electrochemical characterization of new lead-free ferroelectric
Ba_{0.975}Ho_{0.017}(Zr_{0.2}Ti_{0.75})Sn_{0.05}O₃ ceramic. Application to Bezacryl Oxidation Under
Solar Light**

S. Smail ^a, G. Rekhila^{b,1}, K. Taïbi ^a, A. Lahmar ^c and M. Trari ^b

^aLaboratoire de Cristallographie-Thermodynamique, Faculté de Chimie, U.S.T.H.B., BP32, Al Alia, 16111, Alger, Algeria.

^bLaboratoire de Stockage et de Valorisation des Energies Renouvelables, Faculté de Chimie, U.S.T.H.B, BP32, Al Alia, 16111, Alger, Algeria.

^cLaboratoire de Physique de la Matière Condensée (LPMC), Université de Picardie, Jules Verne, Pôle Scientifique, 33 rue Saint-Leu, 80039 Amiens Cedex 1, France.

Abstract

Ba_{0.975}Ho_{0.017}(Zr_{0.20}Ti_{0.75})Sn_{0.05}O₃ (abbreviated BHZ20TS) was elaborated by solid-state reaction at high temperature. The X-ray diffraction pattern, refined by the Rietveld method, indicated that the ceramic has a perovskite structure with a cubic symmetry. The Scanning electron microscopy revealed a high density and low porosity with reduced particle sizes upon substitution of Ba²⁺ by the rare earth ion Ho³⁺. The dielectric study as a function of temperature (-150 – 200 °C) and frequency (10² - 10⁶ Hz) showed relaxor ferroelectric behavior. The modified Curie-Weiss law allowed us to evaluate the diffuse phase transition parameters. BHZ20TS obeys the empirical Vogel–Fulcher relation which confirms the relaxor behavior of this composition. With an optical band gap of 2.56 eV, BHZ20TS is attractive for photocatalytic applications. The capacitance-potential (C⁻² - E) characteristic plotted in Na₂SO₄ (0.1 M) indicates n type behavior with a flat band potential (E_{fb}) of -0.60 V_{SCE} and electronic density (N_A) of 2.2×10¹⁶cm⁻³. The semicircle in the Electrochemical Impedance Spectroscopy (EIS) measured in the range (10⁻³ – 10⁵ Hz) is ascribed to the bulk material BHZ20TS (80 kΩ cm²) with a constant phase element (CPE) and a depletion angle of -5°. As application, the oxide was tested with success for the photooxidation under solar light of Bezacryl (BEZ), a hazardous dye. The energy band diagram shows an electron transfer from the conduction band of BHZ20TS to dissolved oxygen, generating O₂[•] and OH[•] radicals,

¹ Corresponding author.

E-mail address: rekhilagarib@gmail.com (G. Rekhila) ; mtrari@usthb.dz(M. Trari)

responsible of the BEZ mineralization whose disappearance was followed by UV-Vis spectrophotometry. An abatement of 60% is obtained in BEZ solution (10 mg L^{-1}) within 100 min under a solar irradiance of 97 mWcm^{-2} ; the mineralization obeys a first order kinetic model with a half photocatalytic life of 57 min.

Keywords: relaxor $\text{Ba}_{0.975}\text{Ho}_{0.017}(\text{Zr}_{0.20}\text{Ti}_{0.75})\text{Sn}_{0.05}\text{O}_3$; Dielectric ; Photocatalysis; Bezacryl ; Solar light

1- Introduction

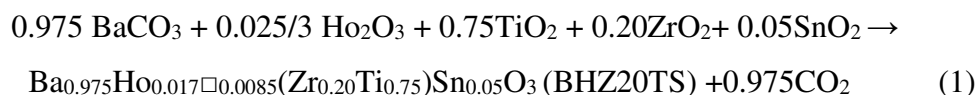
The photocatalysis is used in many domains ranging from the wastewater treatment to disinfection passing by air purification and water splitting [1-6]. To this end, numerous works have been intended for this research field on materials having a chemical stability, environmentally friendly characteristics and good photo activity [7]. However, most of the known photocatalysts like TiO_2 [8-10], ZnO [11] and SnO_2 [12] have some drawbacks; one can cite their weak photo response under visible light and are active only under UV irradiation [13, 14], with a high rate of charge carrier recombination due to their low carriers mobility. These constraints have led to the search of new photocatalytic materials being effectively operational over the visible domain. Among the candidates, the ferroelectric oxides have shown interesting aptitudes in photocatalysis [15] and are well known for their spontaneous polarization responsible of the internal dipole field. The neutralization of this latter by a depolarization field causes the displacement of the holes toward the negatively charged surface while the electrons migrate in the opposite side of the surface, positively charged. Consequently, the separation of electron/hole (e^-/h^+) pairs by the electric field prevents the recombination and improves the lifetime of the charge carriers, resulting in a higher photo activity. This desirable photocatalytic property is observed in conventional ferroelectrics and becomes more amplified in the so-called relaxor ferroelectric materials. The latter's are renowned by the existence of a dielectric peak whose maximum permittivity moves toward high temperatures when the frequency of the applied electric field augments. In addition, the relaxor behavior was generated by the presence of polar nano-domains with an imbalance of electric charge, leading to a local polarization responsible of the frequency dispersion [16]. This polarization should favor the separation of the photo-generated (e^-/h^+) pairs, thus increasing the photo-electrochemical conversion. Indeed, this hypothesis was confirmed by recent studies carried out in our laboratories on different compositions [17-19]. Thus, in continuity this work follows on from the previous one and concerns the study of new

compositions derived from the perovskite BaTiO₃. The reported composition was obtained by hetero-valent substitution at the Ba site (Ba²⁺-Ho³⁺) and a double homo-valent substitution on the Ti site (Ti⁴⁺-Zr⁴⁺-Sn⁴⁺). This composition abbreviated BHZ20TS, characterized by the change of Zr content when substituting Ti⁴⁺ for Zr⁴⁺ (the Sn⁴⁺ content being kept constant). It should be noted that the value $x = 0.20$ corresponds to the Zr limit concentration between classical ferroelectric zone (< 0.20) and relaxor zone (> 0.20) of Ba(Ti_{1-x}Zr_x)O₃ (BZT) compositions [20-22]. The choice of elements Ho, Zr and Sn is related to their capacity to promote the relaxor ferroelectric behavior. In addition, rare earth dopants such as Ho are well known for their ability to reduce the dielectric losses, improve the electrical properties and induce relaxor behavior in the ceramics [23-25]. In addition, they possess large dielectric constants, thus extending the depletion width where the electron/hole (e⁻/h⁺) pairs are separated, an attractive property for the solar applications [26]. To achieve our objective, we first examined the microstructural, structural and dielectric behaviour of our samples. After that, we studied the photo-electrochemical characteristics of the relaxor ferroelectric BHZ20TS in order to test its ability to oxidize Bezacryl a dangerous and persistent dye under sunlight. Indeed, this ferroelectric was positively tested for the formation of (e⁻/h⁺) pairs, involved in the reactive radicals O₂[•] and/or OH[•] in the conduction and valence bands.

2- Materials and methods

2.1 Solid state synthesis

The starting compounds were powders of BaCO₃, Ho₂O₃, TiO₂, ZrO₂ and SnO₂ all from Sigma-Aldrich with a very high purity (>99.99%). BHZ20TS material has been synthesized by the conventional mixed oxide method according to the following chemical reaction:



where “ \square ” symbolizes the vacancy produced through the reaction at high temperature.

The starting oxides were accurately weighed in molar proportions, then mixed and ground for 2 h in an agate mortar. Afterwards, they were heat treated under air atmosphere at 1170 °C for 24 h. After this heat treatment, the mixture is naturally cooled down to room temperature. Then, the mixture is again well ground and then pressed under 500 MPa into pellets 13 mm in diameter and about 1 mm thickness. The resulting disk shaped ceramics were sintered at 1400 °C for 4 h under an air atmosphere with a heating/cooling rate of 5 °C/min on an alumina plate.

2.2 Characterizations

The crystal structure of the sintered pellets was examined by were achieved by means of a D8 Advance X-ray diffractometer (Vantack detector). The data were collected at room temperature using $\text{CuK}_{\alpha 1+2}$ radiation ($\lambda = 1.541 \text{ \AA}$) in the 2θ range ($20 - 80^\circ$). The phase identification was done by comparison of the diffraction patterns with the reference Cards of the JCPDS Powder Diffraction File. The lattice constants were refined by using the Rietveld method. The analysis was accomplished by using the Fullprof [27] database incorporated in Win PLOTR software [28].

The scanning electron microscopy (SEM) was used to observe the microstructure. For this purpose, a Philips XL30 type scanning electron microscope has allowed to examine the microstructures of the sintered samples. The dielectric measurements were carried out on the sintered ceramic discs after depositing silver paste on the two surfaces. A Solartron Impedance Analyzer SI 1200 permitted the measurement of the permittivity and dielectric loss as a function of both temperature and frequency using.

The photo electrochemical properties were studied in a standard Pyrex cell with Pt as emergency electrode and SCE as reference in Na_2SO_4 (0.1 M) solution; the capacitance measurement of the working electrode was carried out at a frequency of 10 kHz. Such value is large enough to ignore the double layer capacitance in the electrolyte. The electrochemical impedance spectroscopy (EIS) was performed with small amplitude wave signals in the frequency region ($10^{-2} - 10^5 \text{ Hz}$). The photocatalytic experiments were done in batch mode in an open Pyrex reactor directly exposed to solar light. The solubility of Bezacryl (BEZ) in water is high. The powder catalyst (50 mg) was suspended in 100 mL of BEZ solution at 50 mg/L at pH ~ 7 ; the dark adsorption took place overnight. After each experiment, the powder was centrifuged (3000 rpm, 15 min) to separate the catalyst from the solution for the chemical analysis.

The detection limit with a maximum sensitivity enhances both the selectivity and resolution between the analyzed molecules and degradation products. The BEZ concentration was controlled by UV-Visible spectrophotometry ($\lambda_{\text{max}} = 415 \text{ nm}$); it was deduced by linear interpolation from a calibrated curve.

3- Results and discussion

3.1 Microstructure

In order to evaluate the influence of the rare earth (Ho^{3+}) on the microstructural and ferroelectric behavior of the ceramic BHZ20TS, SEM image and histogram related to the distribution grain size were carried out (Fig. 1). As can be perceived, the sample with a high density and low porosity is obtained. In addition, the particles appear in spherical shapes with a relatively high grain size ($\sim 10 \mu\text{m}$). Compared to the microstructure of the undoped BZT solid solution [29], the grain growth seems to be inhibited and the grain size is reduced by the addition of very small quantities of Ho^{3+} , thus causing a considerable reduction in the grain size of BHZ20TS. Was confirmed by other authors [30] who affirmed that for a same system, materials with low grain size behave like conventional ferroelectric and crystallize in a tetragonal symmetry. On the other hand, the samples with higher grain size revealed a ferroelectric relaxor behavior, characterized by a cubic symmetry, which is the case of the compound BHZ20TS.

3.2 Room temperature X- ray diffraction analysis

The formation of BHZ20TS was confirmed by XRD analysis performed at room temperature. A pseudo-Voigt profile function has allowed to describe the peak shape, starting with atomic positions taken from BaTiO_3 [31]. We noticed that the XRD profile of BHZ20TS reveals only the peaks belonging to the perovskite phase with a cubic symmetry. Thus, the structural refinement was achieved in the space group Pm-3m. The observed, calculated and the difference of the XRD profiles for BHZ20TS are illustrated in Fig. 2; all reflection peaks of the XRD patterns are indexed which spacing suggests that BHZ20TS has a cubic symmetry at room temperature. Table 1 exhibit the lattice parameters, the volume and the refinement reliability factors. Comparatively to BaTiO_3 as reference, it was found that the incorporation of Zr and Sn in BHZ20TS leads to an increase of the lattice parameters (a) and volume (V). These variations are undoubtedly related to substitution of Ti^{4+} by the bigger Zr^{4+} and Sn^{4+} ($r_{\text{Ti}^{4+}} = 0.605 \text{ \AA}$, $r_{\text{Sn}^{4+}} = 0.690 \text{ \AA}$ and $r_{\text{Zr}^{4+}} = 0.720 \text{ \AA}$ in 6-coordination [32]). Table 1 show also the relative high values of the reliability factors agree with the nanoscale atomic disorder existing in the ferroelectric relaxor compounds [33]. The refined atomic positions and isotropic shift parameters are summarized in Table 2. This shows that the ions Ba^{2+} or Ho^{3+} are located in the same A-site with a fractional percentage. Besides, from the analysis of the various inter-atomic distances, it was observed that the $\text{Ti}^{4+}/\text{Zr}^{4+}/\text{Sn}^{4+}$ cations at the B-sites

are octahedrally coordinated with the oxygen atoms to form $(\text{Ti}^{4+}/\text{Zr}^{4+}/\text{Sn}^{4+})\text{O}_6$ octahedra sharing common corners.

3.3 Dielectric study

Fig.3 showed the thermal variation of the permittivity and dielectric losses at different frequencies for the BHZ20TS composition. This latter is distinguished by a particular ferroelectric behavior. Indeed, the temperature and frequency dependences of the dielectric permittivity (ϵ'_r) present a single and broad peak with a frequency dispersion for $T < T_m$ (T_m being the mean temperature of the maxima of permittivity ϵ'_r). In addition, the temperature T_m is shifted toward higher values as the frequency increases. On the other hand, this evolution with only one phase transition was reported previously for numerous compositions derived from BaTiO_3 . In fact, BaTiO_3 and related compositions presents three structural transitions: Rhombohedral \rightarrow Orthorhombic \rightarrow Tetragonal \rightarrow Cubic. When the composition deviates from BaTiO_3 and regardless of the type of ionic substitution, the orthorhombic and tetragonal ferroelectric phases disappear leading to a single ferroelectric-para electric cubic phase transition [30]. Moreover, we observe at the temperature T_m (182 K) a high permittivity maximum and low dielectric losses ($\epsilon'_{\text{rmax}} = 4853$; $\text{tg}\delta = 0.03$). These values remain important near room temperature ($\epsilon'_{\text{rmax}} \sim 2000$; $\text{tg}\delta \sim 0.03$) due to the spread of the dielectric peak (see Fig.3 and Table 3)

All these dielectric properties are typical of a diffuse phase transition and ferroelectric relaxor behavior.

3.3.1 Diffuse phase transition parameters

3.3.1.1 Curie-Weiss law approach

The Curie-Weiss (C-W) law allows the description of the thermal evolution of the permittivity in the dielectric materials, according to the following relation:

$$\frac{1}{\epsilon'_r} = \frac{T - T_0}{C} \quad (T > T_0) \quad (2)$$

where C is the Curie constant and T_0 the C-W temperature. Regarding a ferroelectric material, the decreasing part of the curve in the paraelectric region evolves according to the C-W law. In this region, the plots $1/\epsilon'_r = f(T)$ make it possible to determine the Curie constant and the C-W temperature. Fig.4 illustrates the thermal evolution of the inverse of the permittivity

recorded at 10 kHz as well as the adjustment the experimental data by Eq. (2) for BHZ20TS. Table 3 shows some ferroelectric characteristic parameters relating to BHZ20TS where it appears that the temperature T_0 is greater than T_m . The values $T_0 > T_m$ confirm the deviation from C-W law. This effect is specific to the ferroelectric materials with a diffuse phase transition and relaxor behavior.

3.3.1.2 Diffusion coefficient (γ) and modified Curie-Weiss law

To materialize the deviations from the C-W law observed in the ferroelectric relaxor materials, empirical modifications were made to C-W law to describe the thermal evolution of the permittivity for $T > T_m$. We then speak of the modified C-W law [34]:

$$\frac{1}{\epsilon'_r} - \frac{1}{\epsilon'_{rmax}} = \frac{(T-T_m)^\gamma}{C} \quad (3)$$

where ϵ'_m is the peak value of ϵ'_r , C a constant and γ is the diffuseness exponent. The phase transition character; the value γ ($= 1$) corresponds to a normal ferroelectric while γ ($= 2$) is for a typical relaxor transition with a complete diffuse phase [35]). The plot between $\log(1/\epsilon'_r - 1/\epsilon'_m)$ and $\log(T-T_m)$ for BHZ20TS at 1 kHz is depicted in Fig. 5. The mean value of the diffusivity γ was extracted from these plots by fitting a straight-line equation. Table 3 showed a relatively high γ value (> 1) which is compatible of a diffuse phase transition and relaxor behavior. It should be noted that the result obtained in this work present much similarities with this announced by Bhargavi et al. about the Gd-BaZr_{0.05}Ti_{0.95}O₃ ceramic study [36].

3.3.1.3 Temperature variation of maximum permittivity

The quantities ΔT_m is also used to evaluate the degree of diffusion of the phase transition.

$$\Delta T_m = T_{dev} - T_m \quad (4)$$

T_m is the maximum temperature of ϵ'_r ; T_{dev} is the temperature from which begins the deviation from the C-W law. The value obtained for BHZ20TS ($\Delta T_m \sim 124$) indicates the high diffuseness of the phase transition (see Table 3).

3.3.2 Relaxors parameters

The relaxor parameter taking into account the frequency dispersion corresponds to the ratio $\Delta\varepsilon'_r/\varepsilon'_r$, such as:

$$\Delta\varepsilon'_r/\varepsilon'_r = (\varepsilon'_r(10^2\text{Hz}) - \varepsilon'_r(10^5\text{Hz})) / \varepsilon'_{\text{rmax}}(10^2\text{Hz}) \quad (5)$$

The corresponding value is all the higher as the composition moves away from a conventional ferroelectric and therefore the relaxor effect is strong. In our case, the ratio $\Delta\varepsilon'_r/\varepsilon'_r = 0.114$ agrees with the characteristic of a frequency dispersion. This value implies the significant difference between the temperatures of the permittivity maximum and consequently confirms the relaxor behavior of BHZ20TS.

3.3.3 Analysis by the Vogel-Fülcher theory

The Vogel-Fülcher relation can be expressed by the following equation: [37]

$$f = f_0 \exp \frac{-E_a}{k_B(T_m - T_g)} \quad (6)$$

where f_0 is the attempt frequency, E_a a measure of average activation energy, k_B the Boltzmann's constant and T_g the freezing temperature.

Fig.6 shows the plot of $\log(f)$ vs T_m for the relaxor sample BHZ20TS. The experimental curve was fitted using the above Vogel-Fülcher formula. The shift of T_m to lower values with decreasing the frequency obeys to the Vogel-Fülcher law. This is known to be one of the characteristics of relaxor systems; the fitting parameters of this relation were $T_g = 158$ K, $E_a = 0.024$ and $f_0 = 1.1 \times 10^8$. The close agreement of the data with the Vogel-Fülcher relationship suggests a relaxor like behavior for BHZ20TS.

3.4 Electrochemical and photocatalytic investigations

The optical properties of the relaxor BHZ20TS are studied from the diffuse reflectance. The photon ($h\nu$), absorption coefficient (α) and forbidden band (E_g) are related by the relation:

$$(\alpha h\nu)^{1/m} = A (h\nu - E_g) \quad (7)$$

The exponent is equal to 0.5 and 2 respectively for direct and indirect transitions. The E_g value of the perovskite BHZ20TS (2.56 eV), determined from the extrapolation of the line $(\alpha h\nu)^{0.5}$ to $h\nu$ axis (Fig. 7), is close to that obtained for similar perovskites [38,39].

Unlike the electrical conductivity, the defect states and grain boundaries have no influence on the thermo-power (S) which accounts for the intrinsic component. The negative value of S indicates that the dominant charge carriers are electrons (Fig. 8), coming mainly from oxygen deficiency with formation of vacancies. The constancy of S with temperature indicates an electron density thermally activated with a mobility more or less constant ($\sim 0.1 \mu\text{V K}^{-1}$) and such value is compatible with an electron density (N_D) of $\sim 10^{18} \text{ cm}^{-3}$ (see below).

The electrochemical study is crucial in photocatalysis since it allows positioning the energy of the valence band (VB) and conduction band (CB) in the electrochemical scale and predicts the interfacial reactions at the junction BHZ20TS/electrolyte. The intensity-potential $J(E)$ curve of the perovskite looks like a chemical diode (Fig. 9) and does not exhibit an hysteresis with a decomposition voltage exceeding 3 V, characteristic of high over potentials. A small reduction peak at $\sim -0.4 \text{ V}$ is due to the superoxide formation ($2 \text{ H}_2\text{O} + \text{O}_2 + 2 \text{ e}^- \rightarrow \text{H}_2\text{O}_2 + 2\text{OH}^-$) and which disappears under N_2 flow. Below $\sim -1.2 \text{ V}$, the current increases continuously with no plateau region, due to hydrogen liberation confirmed by evolved bubbles gas on the electrode surface. The polarization resistance ($=173.2 \text{ k}\Omega$) and the small exchange current J_0 ($0.06 \mu\text{A cm}^{-2}$) indicate a long-lived perovskite in the working medium (Na_2SO_4) (Fig. 9 Inset). The current J_0 is equivalent to the rate constant of the electron transfer for zero potential.

The flat band potential (E_{fb}) is of paramount utility in the photo-electrochemical conversion and is accurately determined from the capacitance measurement; its value (-0.60 V) is deduced by extrapolation of the line ($C_{sc}^{-2} - E$) to infinite capacitance ($C^{-2} = 0$) (Fig. 10):

$$\frac{1}{C^2} = \left(\frac{2}{\epsilon \epsilon_0 e S^2 N_A} \right) (E_{fb} - E) \quad (8)$$

Where the symbols have their usual significations. The electronic density (N_A) of $2.2 \times 10^{16} \text{ cm}^{-3}$ was determined from the slope dC^{-2}/dE . The energy diagram of the junction BHZ20TS/solution, plotted from the photo-electrochemical characterization, predicts from a thermodynamic point of view the degradation of the BEZ solution upon solar irradiation. The

BEZ mineralization occurs by the reactive radicals $O_2^{\bullet-}$ and OH^{\bullet} respectively in the conduction band (-0.49 V) and valence band (2.04 V); both levels $O_2/O_2^{\bullet-}$ and $^{\bullet}OH/H_2O$ are inside the gap region [40].

BHZ20TS is a wide band gap semiconductor, suitable for the BEZ mineralization under solar light. The potentials of VB and CB are easily computed from the relations:

$$E_{BC} = 4.75 - e \times E_{fb} - E_a^2 \quad (9)$$

$$E_{BV} = E_{BC} - E_g \quad (10)$$

4.75 is the energy of SCE with respect to vacuum; the bands (VB: +1.76 V / 6.51 eV) and (CB: -0.80 V / 3.95 eV) derive respectively from O^{2-} : $2p$ and Ti^{4+} : $4s$ orbitals.

The EIS representation of the interface BHZ20TS / Na_2SO_4 solution measured after stabilization of the free potential, exhibits a perfect semicircle assigned to the faradic charge transfer (Fig. 11). The impedance of the system is determined by the depletion region and the large diameter is due to the high bulk resistance R ($80 \text{ k}\Omega \text{ cm}^2$); the center (-4.9° below real axis) suggests an electron hopping by overcoming a small potential barrier. To take into account the non-ideality of the capacity, we have introduced a constant phase element (CPE) due to the roughness of the electrode surface and defect states within the gap region [41]:

$$Z = \{Q(j\omega)^k\}^{-1} \quad (11)$$

Q is a proportionality factor, j the imaginary number ($j = \sqrt{-1}$), ω the angular frequency and the exponent k the homogeneity factor. The low electrolyte resistance ($500 \Omega \text{ cm}^2$) equal to offset from the origin comes from the ionic species ($2 Na^+$ and SO_4^{2-}); the EIS data are fitted by an equivalent electrical circuit (Fig. 11 Inset).

As mentioned in introduction, BEZ is a hazardous dye and its elimination is highly recommended for the protection of the aquatic environment. The perovskite BHZ20TS is promising in such a case owing to its positions of electronic bands and a gap E_g sensitive in

² The activation energy was calculated from the thermal dependence of the electrical conductivity (σ), a value of 0.2 eV was deduced from the plot $\log \sigma$ vs. $1000/T$.

the visible region. The BEZ oxidation can be achieved by a photo-catalytic process according to the following scheme [42, 43]:



The potential of the excited dye is below the conduction band of BHZ20TS and both the photoelectrons and photoholes contribute to the BEZ oxidation by the radicals O_2^\bullet and $\bullet\text{OH}$.

The oxidative species ($\bullet\text{OH}$, O_2^\bullet) attack the dye BEZ, resulting in a partial mineralization to CO_2 and H_2O [44,45].

The UV-Visible spectrophotometry allows to follow the kinetics of BEZ removal; Fig. 12a shows the different spectra recorded over solar illumination time, which do not show secondary products, indicating that their concentrations are below the threshold detection of the equipment. The decay in absorbance at 415 nm (λ_{max}) over illumination indicates an abatement of 60% and the kinetic obeys a first order model with a half photocatalytic life of 57 min (Fig. 12 b):

$$\text{Ln } C_t = -kt + \text{Ln } C_0 \quad (16)$$

Other compositions in the system $\text{Ba}_{0.975}\text{Ho}_{0.017}(\text{Zr}_x\text{Ti}_{1-x})\text{Sn}_{0.05}\text{O}_3$ have been tested successfully in the oxidation of various dyes and the results will be consecutively reported.

4- Conclusion

In summary, the composition $\text{Ba}_{0.975}\text{Ho}_{0.017}(\text{Zr}_{0.20}\text{Ti}_{0.75})\text{Sn}_{0.05}\text{O}_3$ (BHZ20TS) has been prepared by solid state reaction and characterized by SEM and XRD analyses, dielectric and photo-electrochemistry. The SEM image showed a ceramic with a high density and low porosity. The structure refinement showed a cubic symmetry where the ions Ba^{2+} and Ho^{3+} are located in the A-sub lattice site with 12-fold coordination and a fractional percentage. Besides, it was observed that the cations $\text{Ti}^{4+}/\text{Zr}^{4+}/\text{Sn}^{4+}$ occupy the B-site and are octahedrally coordinated with the oxygen atoms. In addition, the relative high values of the reliability factor agrees with the atomic disorder in BHZ20TS ferroelectric composition; the dielectric

investigations showed ferroelectric relaxor behavior. The parameters evaluated from the modified Curie-Weiss law and the Vogel-Fülcher analysis confirmed the diffuse phase transition and the relaxor behavior of the BHZ20TS composition.

The photo-electrochemical characterization, which constitutes the second part of this work, clearly showed the potentiality of the lead-free ceramic BHZ20TS for the photocatalytic dye oxidation because of the widened space charge region and environmentally friendly characteristic. The material showed a good Benzacryl photodegradation, and the kinetic was followed by UV-Visible spectrophotometry. A conversion yield of 60% was obtained in BEZ solution (10 mg L^{-1}) within 80 min upon solar light and the kinetic obeyed a first order model with a half-life of 57 min.

References

1. V. M. A. ã, V. M. Arakelyan, G. E. Shahnazaryan, solar energy **89** 153–163 (2005)
2. M. Nan, B. Jin, C. W. K. Chow, and C. Saint, Water Research **44** 2997–3027 (2010)
3. M. I. Maldonado, J. Blanco, W. Gernjak, S. Malato, P. Ferna, Catalysis Today **147** 1–59, (2009)
4. D. Bahnemann, Solar Energy **77** 445–459 (2004)
5. G. Rekhila. A. Saidani, F. Hocine , S. Habi Ben Hariz, M. Trari, **126** 1–8, (2020)
6. Z. Boukhemikhem, G. Rekhila, R. Brahimi, M. Trari, Journal of Photochemistry & Photobiology, A: Chemistry **394** 112454-5 (2020)
7. K. Cherifi, G. Rekhila, S. Omeiri, Y. Bessekhoud, M. Trari, *Journal of Photochemistry & Photobiology, A: Chemistry*, **368** 290–295 (2019)
8. K. Drew, G. Girishkumar, K. Vinodgopal, and P. V Kamat, J. Phys. Chem. B, **109** 11851–11857 (2005)
9. K. Rajeshwar, M. E. Osugi, W. Chanmanee, and C. R. Chenthamarakshan, Journal of Photochemistry and Photobiology C: Photochemistry Reviews **9** 171–192 (2008)
10. Z. Bensaadi, N. Yeddou-Mezenner, M. Trari, F. Medjene DOI: 10.1016/j.jece.2014.03.025 (2014)
11. R. Brahimi, Y. Bessekhoud, M. Trari, Physica B **407** (2012) 3897–3904 (2018)
12. H. Ali, R. Brahimi, R. Outenzabet, B. Bellal, M. Trari, Thin Solid Films **649** 225–231 (2018)
13. H. A. Zyoud , H. Salah, S. H. Zyoud, S. H. Zyoud, M. H. Helal, N. Qamhieh, A. Hajamohideen, H. Nassar, H. S. Hilal, The Minerals, Metals & Materials Society **73** 404–410 (2021)
14. A. H. Zyoud, A. Zubi, S. Hejjawi, S. H. Zyoud, M. H. Helal, S. H. Zyoud, N. Qamhieh, A. R. Hajamohideen, H. S. Hilal, Journal of Environmental Chemical Engineering, **8** 104038-104049 (2020)
15. M. A. Khan, M. A. Nadeem, and H. Idriss, Surface Science Reports, **71** 1–31 (2016)
16. V. Westphal, W. Kleemann, M. D. Glinchuk Phys. Rev. Lett. **68** 847–850 (1992)
17. A. Kerfah, K. Taibi, S. Omeiri, M. Trari, Solar energy **85** 443–449 (2011)
18. N. Boutal, G. Rekhila, K. Taibi, M. Trari, Solar Energy **99** 291–298 (2014)
19. N. Haddadou, N. Bensemme, G. Rekhila, M. Trari, K. Taïbi, Journal of Photochemistry and Photobiology A : Chemistry **358** 294–299 (2018)

20. Y. Wang, L. Li, J. Qi, and Z. Gui, *Ceramics international* **28** 657–661 (2002)
21. Z. Yu, C. Ang, R. Guo, and A. S. Bhalla, *Materials Letters* **61** 326–329 (2007)
22. C. Ciomaga, M. Viviani, M. T. Buscaglia, V. Buscaglia, L. Mitoseriu, A. Stancu, P. Nanni, *Journal of the European Ceramic Society* **27** 4061–4064 (2007)
23. X. Diez-Betriu, J.E. Garcia, C.Ostos, A.U. Boya, D.A.Ochoa, L. Mestres, R.Perez *Materials Chemistry and Physics*, **125** 493–499 (2011)
24. S. K. Ghosh and S. K. Rout, *Current Applied Physics*, **16** 989–1000 (2016)
25. S. B. Reddy, M. S. R. Rao, and K. P. Rao, *Applied Physics Letters* **22917** 65–68, (2014)
26. G. Rekhila, R. Brahimi, Y. Bessekhoud, and M. Trari, *Journal of Photochemistry and Photobiology A: Chemistry*, **332** 345–350 (2017)
27. A. Boulouf, D. Louer, *J. Appl. Crystallogr.* **24** 987–993 (1991)
28. T. Roisnel, J. Rodríguez-Carvajal, *Mater. Sci. Forum* 118–123 (2001)
29. B. T. O, S. B. Reddy, K. P. Rao, and M. S. R. Rao, *J. alloys and compounds* **481** 692–696 (2009)
30. X. G. Tang, J. Wang, X. X. Wang, and H. L. W. Chan, *Solid State Communications*, **131** 163–168 (2004)
31. H. Kwei and J. L. Billinge, *J. Phys. Chem.* **97** 2368–2377 (1993)
32. A Kerfah, K. Taïbi, A. Guehria-Laidoudi, A. Simon, J. Ravez, *Materials Letters* **42** 189–193 (2000)
33. P.Bonneau, P.Garnier, E.Husson, A.Morell *Materials Research Bulletin* **24** 201–206 (1989)
34. K. Uchino, S. Nomura, *Ferroelectrics* **44** 55–61 (1982)
35. A. A. Bokov, Z.G Ye, *Solid State Communications* **116** 105–108 (2000)
36. G.N. Bhargavi, A. Khare, T. Badapanda, M.S. Anwar, *Applied Physics A* **124** 1–9 (2018)
37. S. J. Jang, L. Eric Cross, *Journal of Applied Physics* **68** 2916 (1990)
38. G. Rekhila, Y. Gabes, R. Brahimi, Y. Bessekhoud, O. Mahroua, and M. Trari, *Journal of Sol-Gel Science and Technology*, **85** 677–683 (2018)
39. G. Rekhila, Y. Gabes, Y. Bessekhoud, M. Trari, *Solar Energy*, **166** 220–225 (2018)
40. Y. Roumila, K. Abdmeziem, G. Rekhila, and M. Trari, *Materials Science in Semiconductor Processing*, **41** 470–479 (2016)
41. V.M.Aroutiounian, V.M. Arakelyan, G.E. Shahnazaryan, G.M. Stepanyan, E.A. Khachatryan, H. Wang, J. A.Turner, *Solar Energy*, **80** 1098–1111 (2006)
42. O. Ouagagui, G. Rekhila, R. Nedjar, and M. Trari, *Journal of Materials Science: Materials in Electronics*, **31** 1257–1264 (2020)
43. O. Ouagagui, G. Rekhila, R. Nedjar, and M. Trari, “*Journal of Photochemistry & Photobiology A : Chemistry* **398** 112610-7 (2020)
44. L. Dermèche, C. Rabia, G. Rekhila, and M. Trari, *Solar Energy Materials and Solar Cells*, **168** 45–50 (2017)
45. D. Amitouche, T. Mazari, G. Rekhila, C. Rabia, and M. Trari, *Journal of Inorganic and Organometallic Polymers and Materials*, 1574-1443 (2019)

Figures

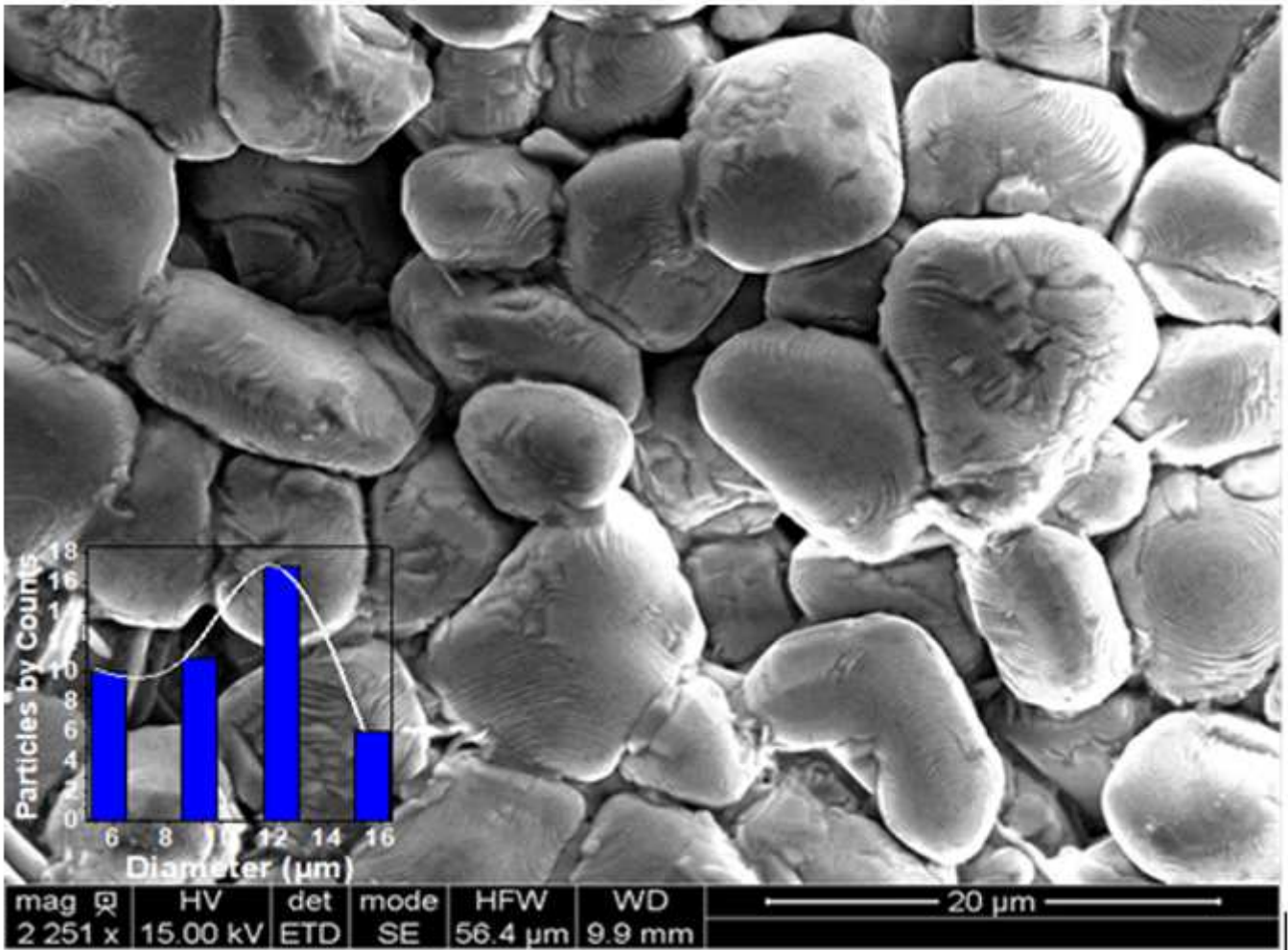


Figure 1

The SEM image for the ceramic BHZ20TS

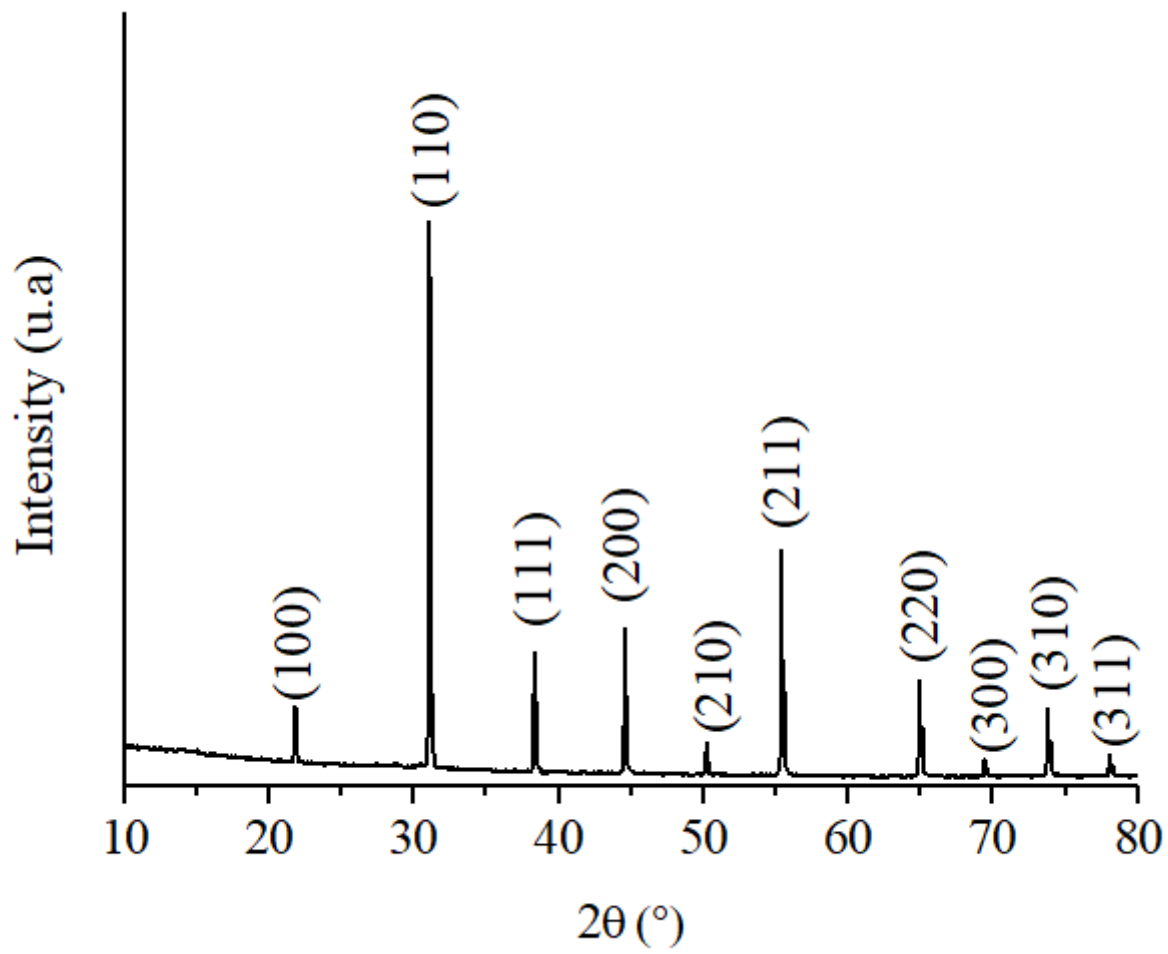


Figure 2

Rietveld profile refinement of the X-ray diffraction data for the ceramic BHZ20TS

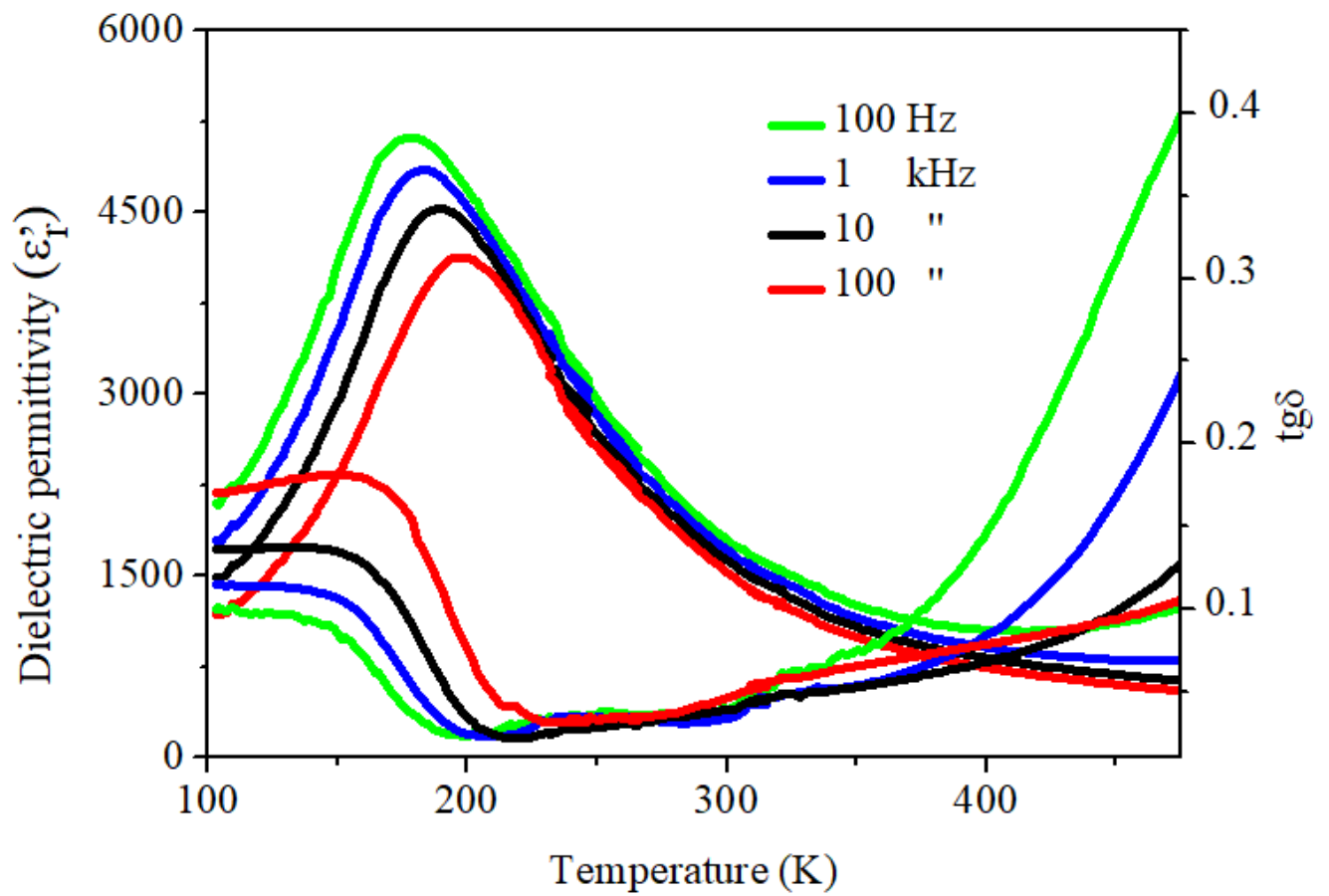


Figure 3

Temperature dependence of the dielectric constant and tangent loss BHTZ20S compositions

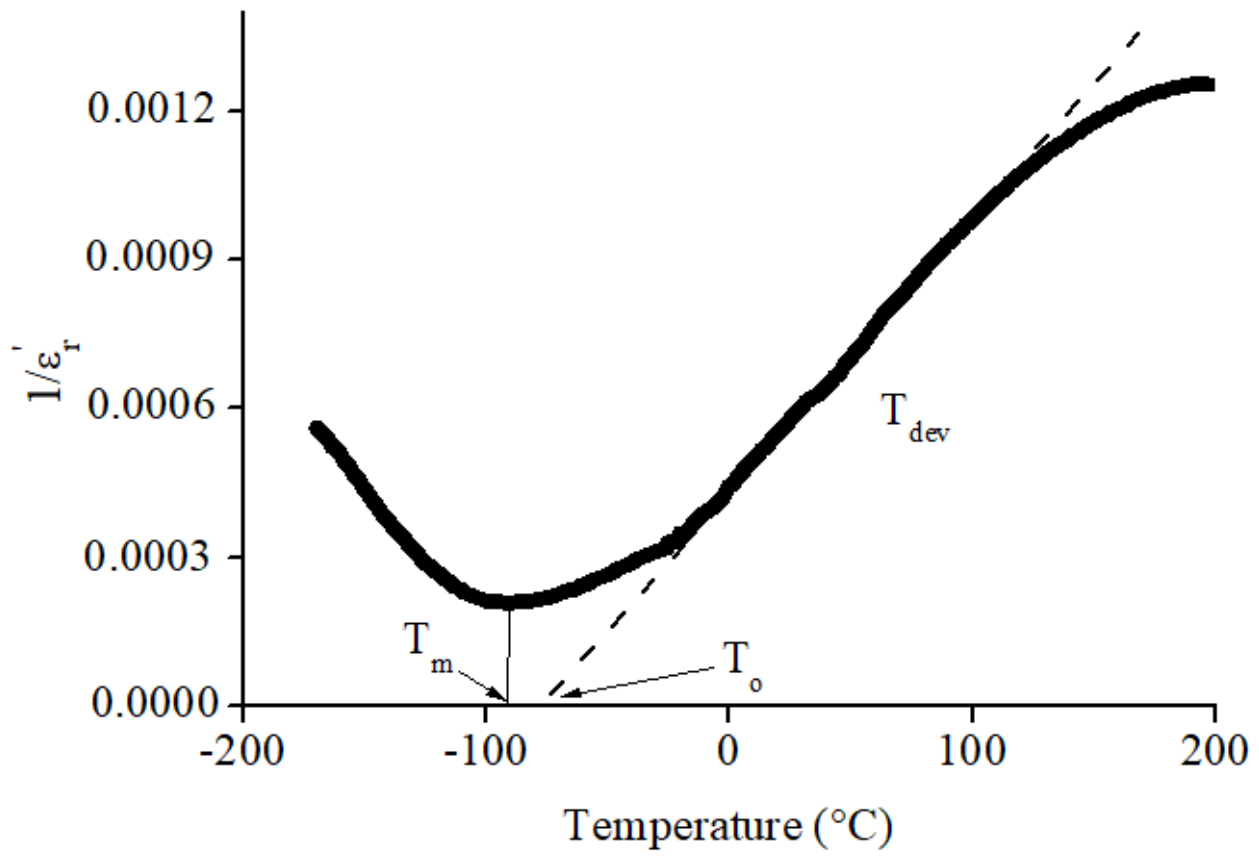


Figure 4

Thermal evolution of the inverse of the permittivity for BHZ20TS compositions

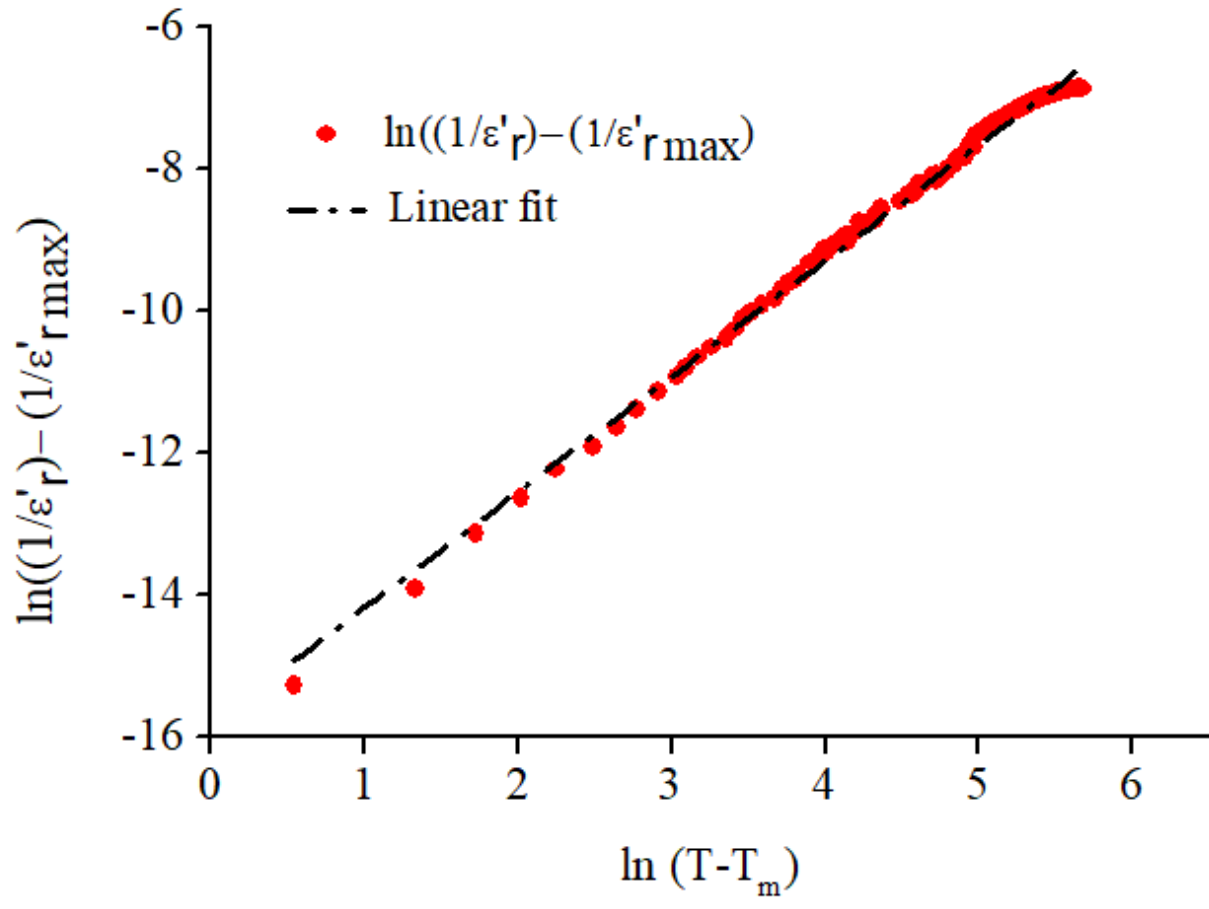


Figure 5

Plots of $\ln(1/\epsilon_r - 1/\epsilon_m)$ versus $\ln(T - T_m)$ at 1 kHz for BHZ20TS

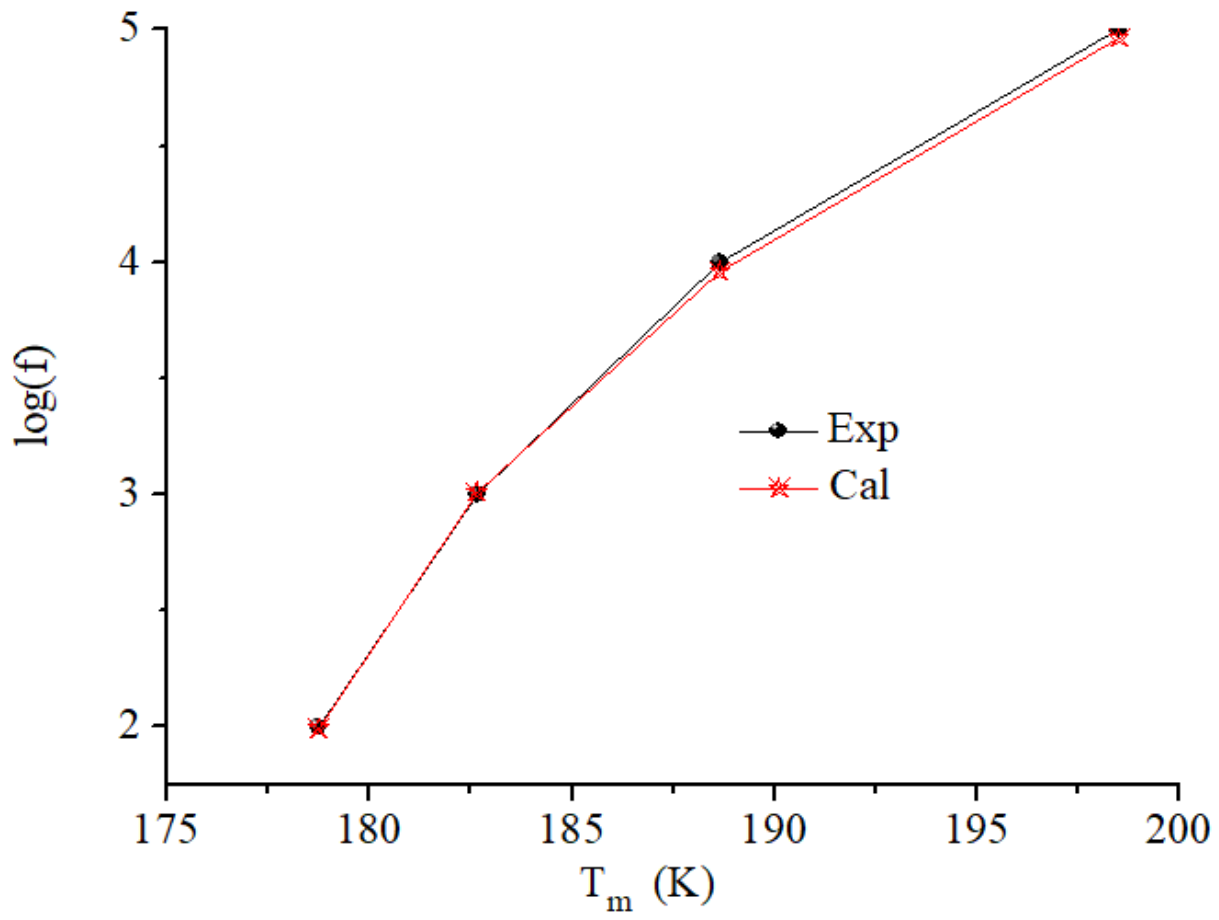


Figure 6

Plots of $\log(f)$ as a function of T_m for the ceramic BHZ20TS (Symbols = experimental data; Solid curve: fitting to the Vogel–Fülcher relation)

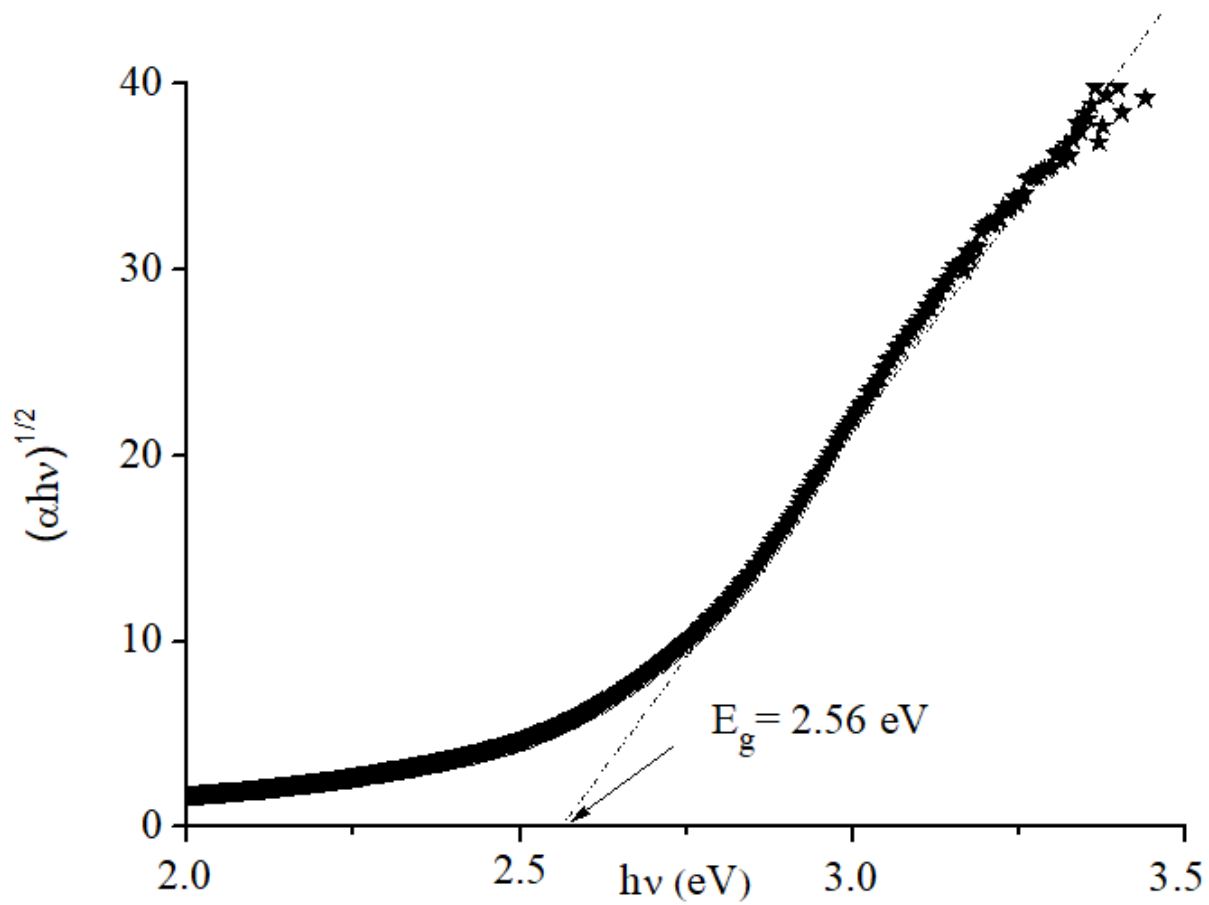


Figure 7

The indirect $(\alpha h\nu)^{1/2}$ optical transitions of BHZ20TS

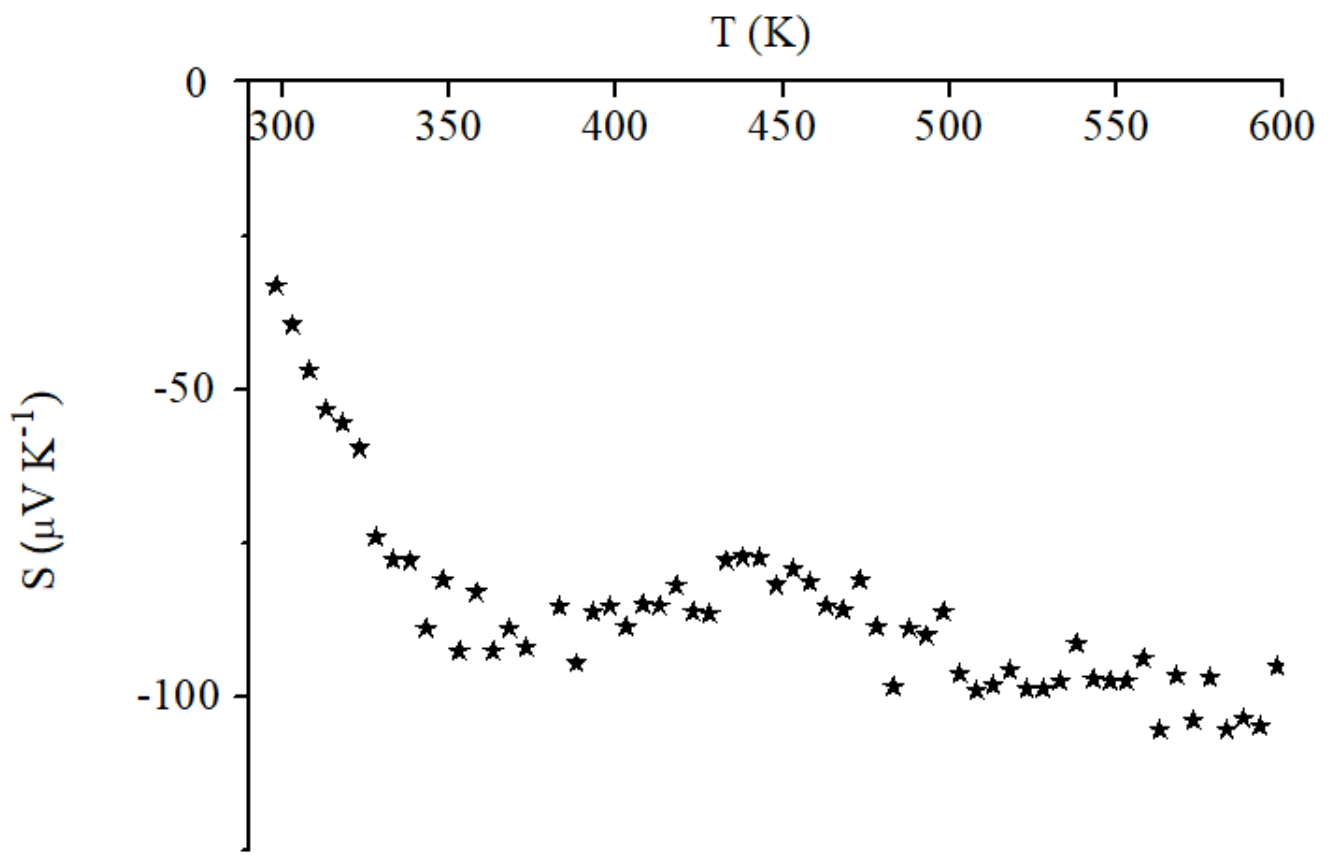


Figure 8

The thermo power of BHZ20TS

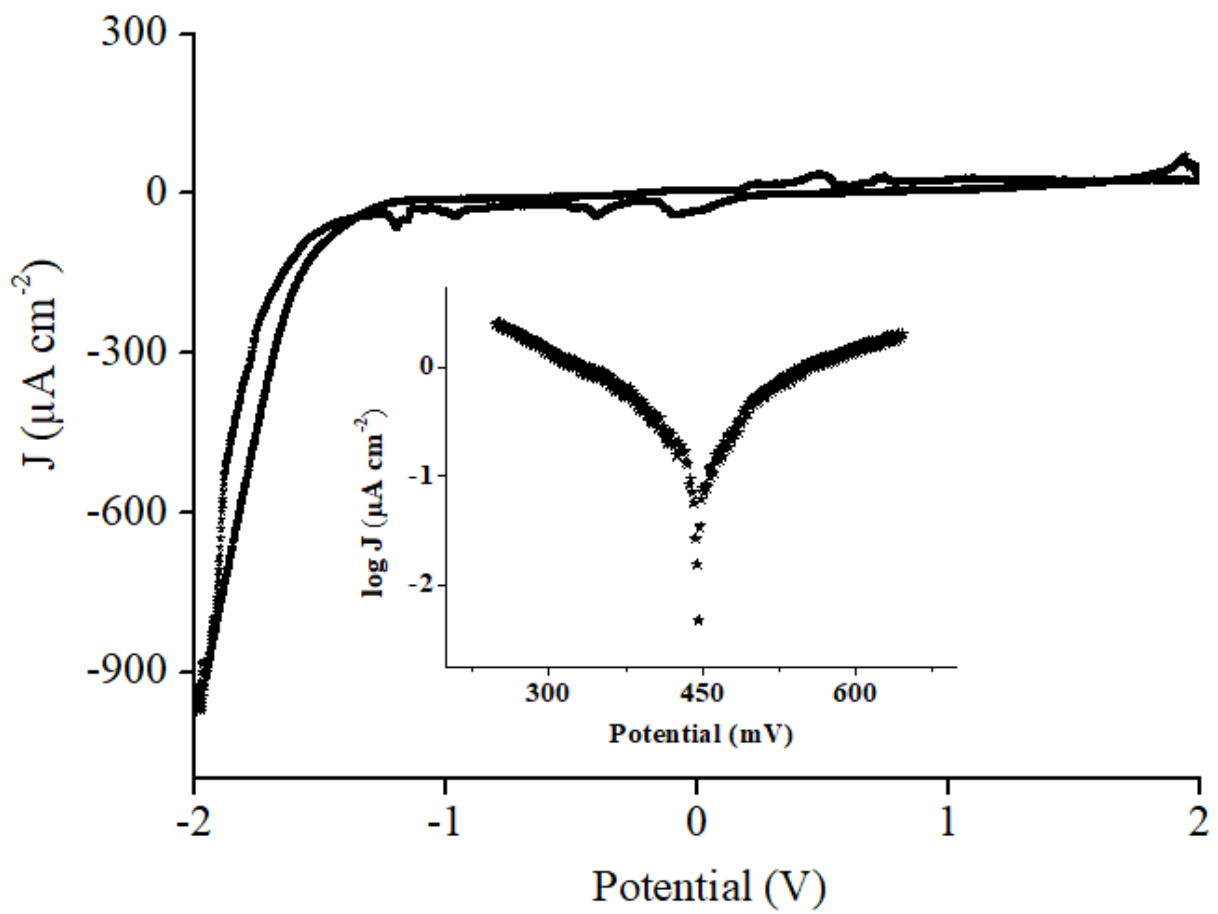


Figure 9

The $J(E)$ characteristic of BHZ20TS plotted in the dark Inset: The Polarization curves in Na_2SO_4 (0.1 M) electrolyte

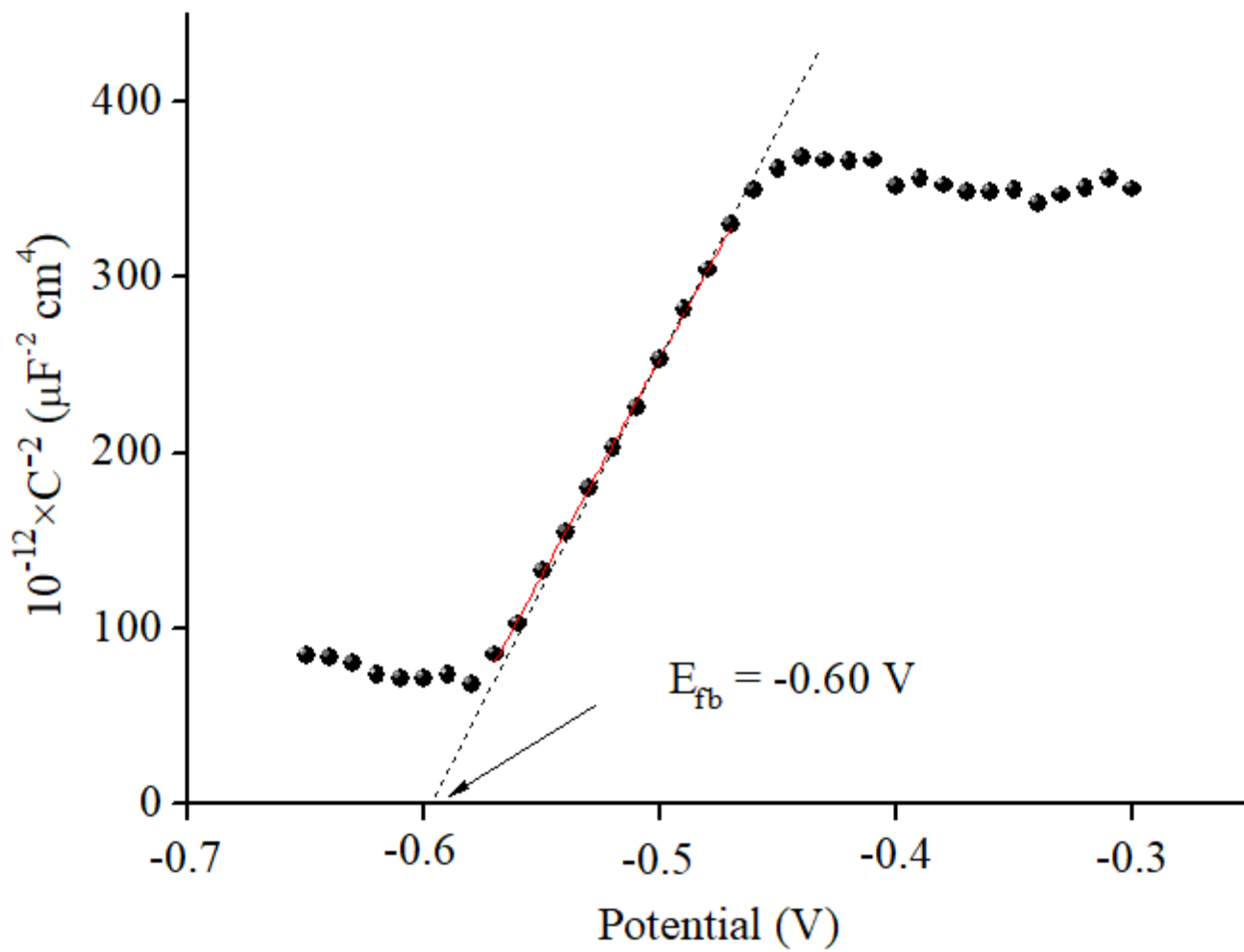


Figure 10

The Mott-Schottky plot of BHZ20TS

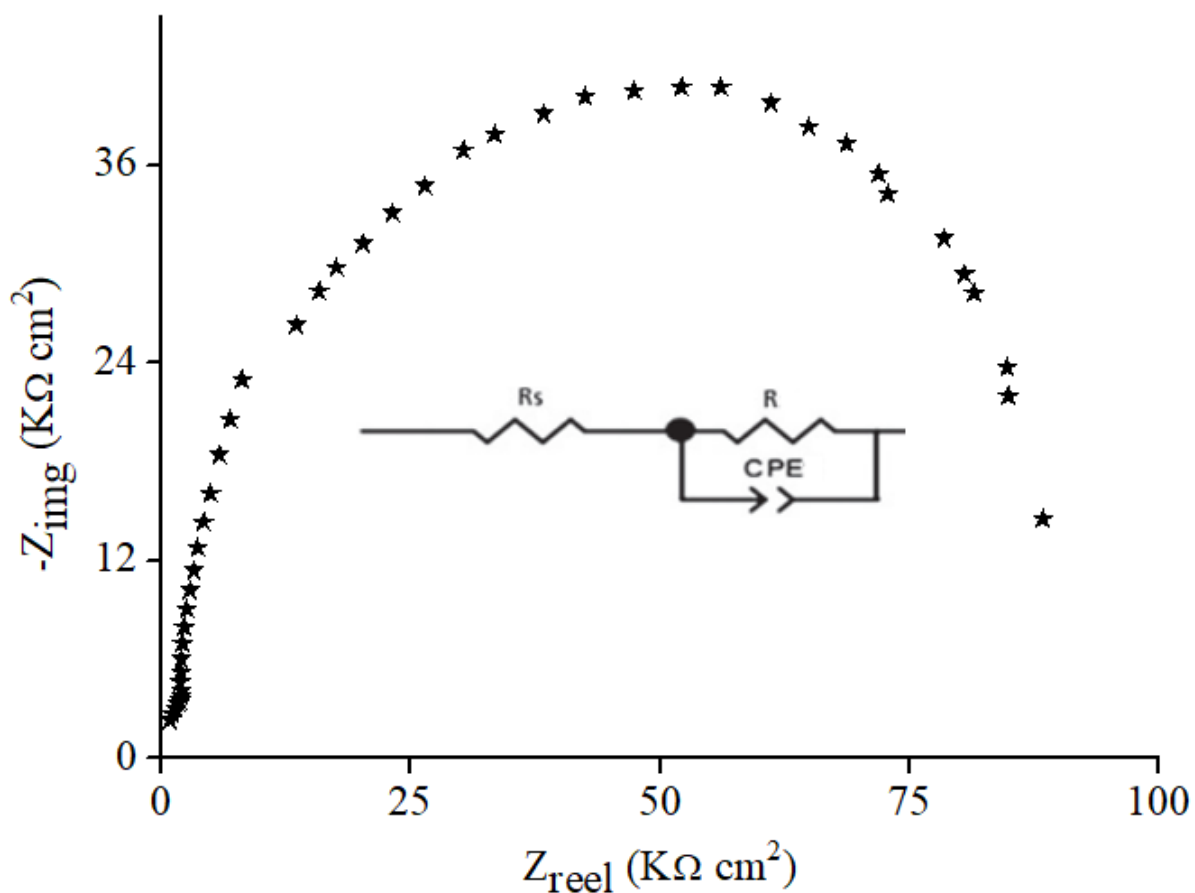


Figure 11

Complex impedance plots in Na_2SO_4 (0.1 M) solution. Inset: the equivalent electrical circuit

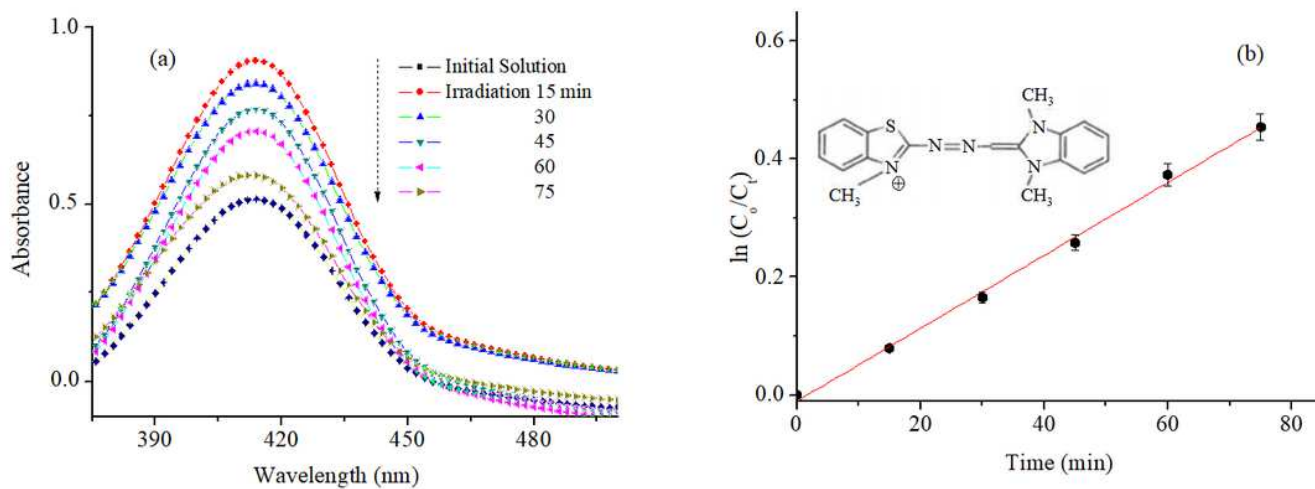


Figure 12

The UV-vis spectra of Bez solutions on BHZ20TS over illumination time. (b) The kinetic plot $\ln C_0/C_t$ vs. time Experimental conditions: catalyst dose: 0.5 g/L; [Bezacryl] = 10 mg L⁻¹; V_{solution} = 100 mL